

Electron injection and acceleration into laser-driven wakefield from a solid overdense plasma target

M. Caetano de Sousa,^{1,*} S. Marini,² M. Grech,³ S. Brunner,⁴ C. Riconda,⁵ and M. Raynaud¹

¹*LSI, CEA/DRF/IRAMIS, CNRS, École Polytechnique, Institut Polytechnique de Paris, F-91120 Palaiseau, France*

²*CEA, IRFU, DACM, Université Paris-Saclay, 91191 Gif-sur-Yvette, France*

³*LULI, CNRS, CEA, Sorbonne Université, École Polytechnique, Institut Polytechnique de Paris, F-91120 Palaiseau, France*

⁴*Swiss Plasma Center, École Polytechnique Fédérale de Lausanne (EPFL), CH-1015 Lausanne, Switzerland*

⁵*LULI, Sorbonne Université, CNRS, CEA, École Polytechnique, Institut Polytechnique de Paris, F-75252 Paris, France*

A laser-plasma acceleration scheme combining electron extraction from a solid overdense target with wakefield acceleration in an adjacent underdense plasma region is presented. A laser pulse excites a diffracted electromagnetic wave at the overdense plasma interface, extracting and pre-accelerating electrons, which are then injected into laser-driven wakefield cavities in the underdense plasma. A parametric study identifies key conditions enabling efficient electron injection and energy gain in this two stage acceleration configuration. Two-dimensional particle-in-cell simulations performed with the SMILEI code show that the proposed scheme produces high quality electron bunches with high amounts of charge and energy at laser intensity $I_0\lambda_0^2 \simeq 3.4 \times 10^{19} \text{ W}\mu\text{m}^2/\text{cm}^2$ ($\lambda_0 = 0.8 \mu\text{m}$). According to the parameters used, the electron beam is accelerated to peak energies of $\sim 150 - 250 \text{ MeV}$ with an estimated charge in 3D of $\sim 50 - 400 \text{ pC}$ integrated over the full width at half maximum energy range, and $\sim 100 - 1800 \text{ pC}$ with energies above 50 MeV .

I. INTRODUCTION

Laser-plasma acceleration has emerged as a promising technique to generate high-energy electron beams (up to $\sim\text{GeV}$) over short distances ($\sim\text{mm}$) in both underdense [1–11] and overdense plasmas [12–33], defined respectively by the plasma density n_e below and above the critical density n_c for a laser pulse of frequency ω_0 . Each regime leads to electron beams with distinct characteristics.

Laser interaction with overdense plasmas can result in electron acceleration through various mechanisms, including vacuum laser acceleration (VLA) [14, 16, 32], direct laser acceleration (DLA) [18, 20, 24–26], as well as resonantly excited relativistic surface plasma waves (SPWs) [15, 17, 19, 21–23, 27–30]. Notably, when the laser interacts with the plasma edge, both SPWs [30, 31, 34] and diffracted waves [33] are excited, each contributing differently to the electron acceleration process. Diffracted waves, specifically, generate strong longitudinal electric fields that propagate in vacuum at the speed of light and decay with the longitudinal distance. These fields enable efficient electron acceleration, with energy gain γ scaling as $\gamma = 2\eta a_0 \sqrt{k_0 \Delta x}$, where a_0 is the normalized laser amplitude, k_0 is the wave number, Δx is the electron displacement from the interaction point, and $\eta \lesssim 1$ (obtained from simulations) is the ratio between the maximum amplitudes of diffracted and laser fields [33].

Laser-overdense plasma interaction mechanisms can drive electron beams with substantial charge (up to nC) and energies in the MeV range over short distances, with acceleration gradients reaching the TeV/m level. However, the resulting electron spectra are typically continuous rather than monoenergetic, limiting their use in applications requiring well-defined beams. In contrast, laser interaction with underdense plasmas excites plasma wakefields that can capture and accelerate electrons up to GeV energies with small energy spread and pC of charge [8, 11]. Efficient acceleration in this regime depends on appropriate electron injection into the accelerating phase of the wake. Mechanisms such as wave breaking [35] and ionization injection [3–5, 36] allow electron self-injection through control of the plasma density profile.

To improve injection into wakefields, alternative configurations involving multi-region targets have been investigated. Zhang *et al.* [37] proposed placing a thin ($\sim \mu\text{m}$) near-critical density layer ($n_e = 4n_c$) in front of an underdense plasma. In this arrangement, the laser pulse extracts electrons from the layer, which are subsequently injected and accelerated in the wakefield excited in the underdense region. Fedeli *et al.* [38] proposed obliquely irradiating an overdense plasma-mirror surface with a laser pulse to extract electrons, which are subsequently accelerated in a nearby underdense plasma by laser-driven wakefield.

This work investigates an integrated laser-plasma acceleration arrangement that combines laser-overdense and laser-underdense plasma interactions. A single laser pulse excites both a diffracted wave at the overdense plasma interface and a wakefield in the adjacent underdense region. The laser-excited diffracted waves efficiently extract and pre-accelerate electron bunches from the overdense plasma, which are subsequently self-

* Current affiliation: Centre Lasers Intenses et Applications (CELIA), Université de Bordeaux-CNRS-CEA, UMR 5107, F-33405 Talence, France

injected into the laser-driven wakefield for further acceleration. Particle-in-cell simulations were carried out for different parameters values. They demonstrate the generation of high-quality, high-energy electron bunches reaching $\sim 150 - 250$ MeV at peak over a propagation distance of $\sim 685 - 975\lambda_0$ (where λ_0 is the laser wavelength), with projected charges in three dimensions of $\sim 50 - 400$ pC in the full width at half maximum (FWHM) energy range, $\sim 100 - 1800$ pC with energies above 50 MeV, and $\sim 100 - 1220$ pC with energies above 100 MeV.

This paper is organized as follows: Section II introduces the setup for the proposed acceleration mechanism and presents the simulations design. Section III analyzes the self-injection and acceleration processes, as well as the electron dynamics. Section IV presents a parametric study identifying the optimum conditions for the proposed acceleration mechanism. Section V details the optimized configurations for electron beam acceleration aiming either at higher energy or higher charge. Finally, Section VI summarizes the findings and discusses possibilities for future works.

II. SETUP AND PARTICLE-IN-CELL SIMULATIONS

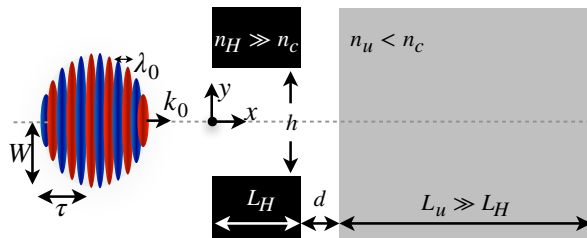


FIG. 1. Laser-plasma interaction setup.

The proposed setup is depicted in Fig. 1. A p -polarized (*i.e.* electric field parallel to the plane of incidence) Gaussian laser pulse propagates in the x -direction with wavelength λ_0 , angular frequency ω_0 and period $\tau_0 = \lambda_0/c$, where c is the speed of light in vacuum and we consider $\lambda_0 = 0.8 \mu\text{m}$. The laser has a waist (minimum radius) $W = 9\lambda_0 = 7.2 \mu\text{m}$, full width at half maximum (FWHM) pulse duration $\tau = 5\tau_0 \approx 13.3$ fs, and normalized vector potential $a_0 = 5$, with $a_0 \equiv eE_0/(m_e c \omega_0)$, E_0 the peak electric field amplitude of the laser pulse, e the electron charge and m_e the electron mass. These parameters correspond to a laser intensity $I_0 \lambda_0^2 \simeq 3.4 \times 10^{19} \text{ W}\mu\text{m}^2/\text{cm}^2$.

The laser sequentially interacts with two plasma regions of different densities. It first propagates through the cylindrical aperture of an overdense plasma target with length L_H ($0 < x \leq L_H$), aperture diameter h in the yOz plane (transverse direction), density $n_H = 100n_c \simeq 1.7 \times 10^{23} \text{ cm}^{-3}$, and plasma wavelength

$\lambda_H \simeq \lambda_0/\sqrt{n_H/n_c} = 80$ nm. Here $n_c = \varepsilon_0 m_e \omega_0^2/e^2$ is the critical plasma density, and ε_0 is the vacuum permittivity. The laser pulse then crosses a vacuum region (gap) of length d ($L_H < x \leq L_H + d$) before entering a uniform underdense plasma with density $n_u \ll n_c$ extending from $x = L_H + d$ to $x = L_H + d + L_u$. The laser is focused at the center of the underdense plasma region $x_f = L_H + d + L_u/2$, enabling a two-stage acceleration mechanism.

To investigate the injection and acceleration dynamics, two-dimensional (2D3V) particle-in-cell (PIC) simulations were conducted using the open-source code SMILEI [39]. In the simulations, both plasma regions consist of cold electrons with $T_e \rightarrow 0$ and a neutralizing background of cold ions with atomic number $Z = 1$. The simulation box extends over $334\lambda_0$ ($= 267 \mu\text{m}$) in the x -direction and $192\lambda_0$ ($= 154 \mu\text{m}$) in the y -direction. The spatial resolution is set to $\Delta x = \Delta y = \lambda_0/128 = \lambda_H/12.8$ ($= 6.25$ nm), such that it is enough to resolve the overdense plasma wave with more than ten points. The simulation time step is chosen to be $c\Delta t = 0.95\Delta x/\sqrt{2}$, corresponding to 95% of the Courant–Friedrich–Lewy (CFL) condition for the standard finite-difference time-domain (FDTD) solver [40]. Each cell initially contains 124 randomly distributed numerical particles of each species in the overdense plasma region and 4 numerical particles of each species in the underdense plasma. Particle boundary conditions in x are removing (left) or thermalizing (right), and thermalizing in the y -direction. It means that particles reaching the left- x boundary are deleted, while particles reaching all the other boundaries have their temperature set to $T \rightarrow 0$. Electromagnetic field boundary conditions are perfectly matched layers (PML), which are open boundary in y and allow laser injection (absorption) from the left (right) x boundary. The final simulation time was set to $t_f = 349\tau_0 \approx 931$ fs.

III. INJECTION AND ACCELERATION MECHANISM

The electron dynamics resulting from the laser-plasma interaction setup discussed in Sec. II is here investigated assuming $L_H = 12\lambda_0 = 9.6 \mu\text{m}$, $h = 10\lambda_0 = 8 \mu\text{m}$, $d = 0$, and $n_u = 0.007n_c \simeq 1.2 \times 10^{19} \text{ cm}^{-3}$. At $t = 0$, the laser pulse reaches the overdense plasma target edge located at $x = 0$. It is focused at $x_f \gg L_H$, such that the laser beam waist in the overdense target region exceeds the aperture radius $h/2$. This geometry leads to a direct interaction of the laser pulse with the overdense plasma edge, exciting diffracted electromagnetic waves that efficiently extract and accelerate electrons from the plasma surface, as depicted in Fig. 2(a) at $t = 16\tau_0$. From Ref. [33], electrons accelerated by such diffracted waves achieve energies up to $\gamma = 2\eta a_0 \sqrt{k_0 L_H}$, with $\eta \lesssim 1$ the ratio between the maximum amplitudes of the diffracted waves and the laser electromagnetic field. In our simulations, electron energies of approximately 28 MeV ($\gamma \approx 55$) are observed,

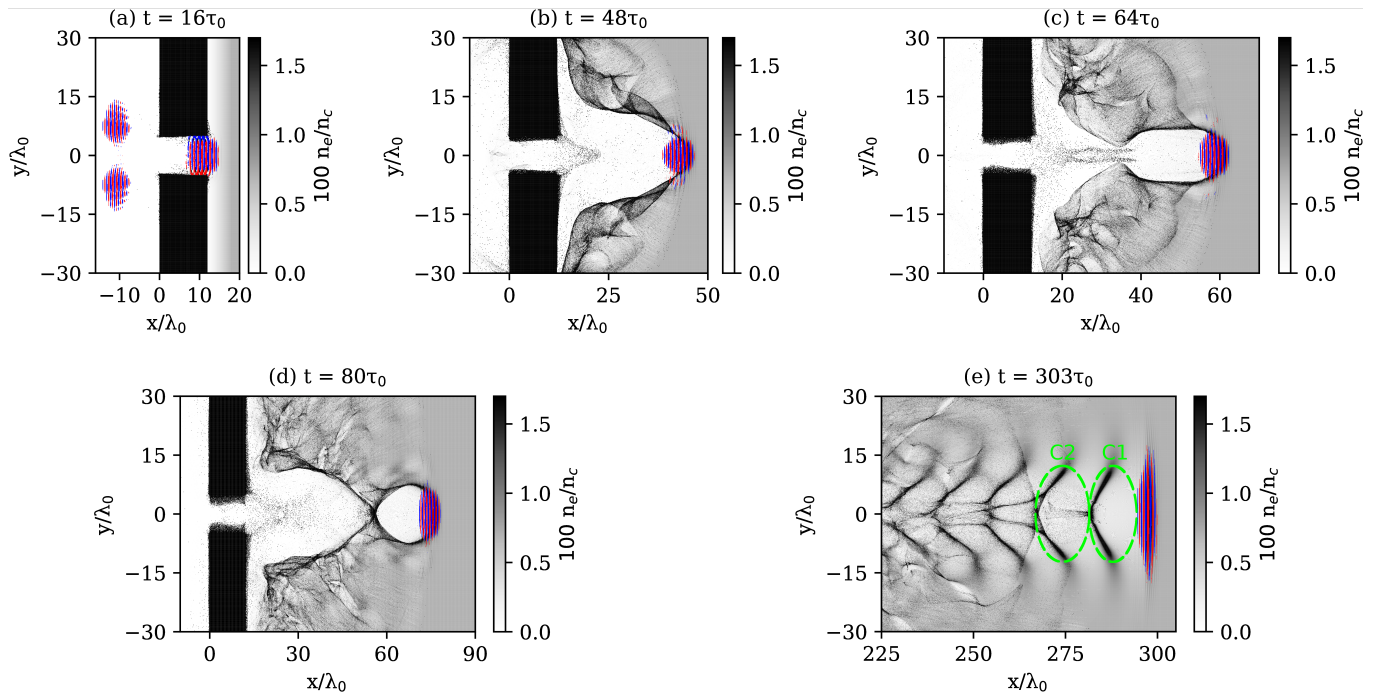


FIG. 2. Spatiotemporal evolution of laser-plasma interaction showing the electron density (grayscale) and the magnetic field component B_z of the laser pulse (red/blue) in x - y space at different instants of time: (a) part of the laser pulse exits the overdense target aperture and part of the laser is reflected by the overdense target above and below its aperture at $t = 16\tau_0$, (b) laser entering the underdense plasma region at $t = 48\tau_0$, (c) formation of the first wakefield cavity at $t = 64\tau_0$, (d) closure of the first wakefield cavity at $t = 80\tau_0$, and (e) multiple wakefield cavities at $t = 303\tau_0$ with the first (C1) and second (C2) cavities indicated by the dashed ellipses in green.

which is slightly weaker than in Ref [33] where the laser is focused at the plasma edge such that the interaction happens at the laser maximum intensity.

Besides being accelerated, electrons from the overdense plasma are also heated by the laser, and remain co-propagating with it as the pulse advances beyond the target, as can be seen in Figs. 2(b)-(d). At $t = 48\tau_0$, Fig. 2(b), the laser pulse has entered the underdense plasma region, with pre-accelerated and pre-heated electrons from the overdense plasma propagating behind it. As the laser advances through the underdense plasma, it exerts a ponderomotive force on the background electrons, forming characteristic wakefield cavities, as illustrated in Figs. 2(c)-(d) at $t = 64\tau_0$ and $t = 80\tau_0$. Persistent electromagnetic fields continue to extract electrons from the overdense target, sustaining their injection into the wakefield structure. By $t = 303\tau_0$, Fig. 2(e) shows that multiple well-defined wakefield cavities are present, all of which can support the formation and acceleration of distinct electron bunches.

Figures 3 and 4 illustrate the electric field structure of the wakefield at two instants of time: $t = 80\tau_0$ and $t = 303\tau_0$ respectively. The longitudinal field E_x is shown in the upper panels Figs. 3(a) and 4(a), while the transverse field E_y is presented in the lower panels Figs. 3(b) and 4(b). At $t = 80\tau_0$, strong longitudinal fields create an accelerating gradient that captures and accelerates elec-

trons coming from the overdense target into the dark blue regions of Fig. 3(a). Simultaneously, the transverse fields provide the focusing forces necessary for beam confinement, as illustrated in Fig. 3(b). By $t = 303\tau_0$, the electric field structures stabilize throughout multiple wakefield periods, maintaining both the acceleration mechanism and radial focusing required for electron bunch formation, as shown in Figs. 4(a) and 4(b).

At $t = 303\tau_0$, most of the charge is concentrated in the two first cavities defined as C1 and C2 in Fig. 2(e). Thus, in the following discussion we will concentrate on the first and second wakefield cavities. Their charge distribution as a function of the electron energy at $t = 303\tau_0$ is shown in Fig. 5. There, the solid red line represents the total electron population (all), the dashed blue line shows electrons originating from the overdense plasma (target), and the dash-dotted green line indicates electrons from the underdense plasma (gas). In the first cavity (C1), Fig. 5(a), all accelerated electrons originate from the overdense plasma, whereas in the second cavity (C2), Fig. 5(b), a combination of electrons from both overdense and underdense plasma is observed. The acceleration of electron bunches with a significant amount of particles from the overdense target validates the proposed setup as an alternative and efficient method for self-consistent electron injection into laser-driven wakefields.

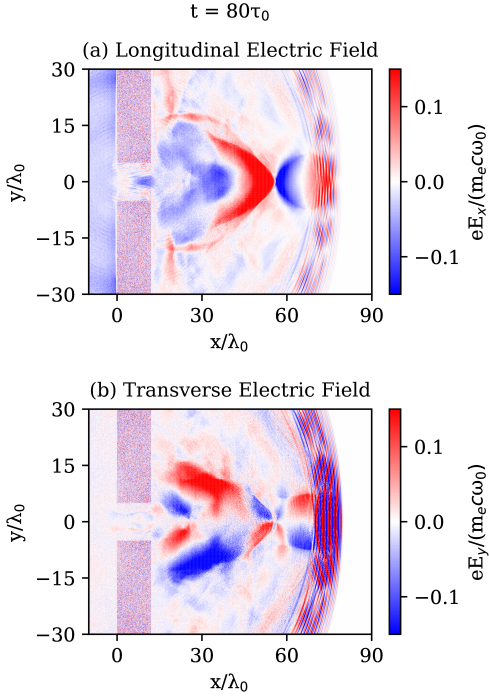


FIG. 3. Electric field in the (a) longitudinal x -direction and in the (b) transverse y -direction at $t = 80\tau_0$.

TABLE I. Beam parameters in the first (C1) and second (C2) wakefield cavities at $t = 303\tau_0$.

Parameter	C1	C2
Maximum Energy (MeV)	71	42
Peak Energy (MeV)	67	37
FWHM Energy Spread (MeV)	6.2	9.6
FWHM Energy Spread (%)	9.3	26
FWHM Divergence (mrad)	168	253
FWHM Transverse Size in y direction (μm)	5.1	7.7
FWHM Normalized Emittance (π mm mrad)	5.6	4.0
Integrated FWHM Charge ($\text{pC}/\mu\text{m}$)	4.1	7.7
From Overdense Plasma (%)	100	67
From Underdense Plasma (%)	0	33
Estimated Total FWHM Charge (pC)	52	81
Integrated Charge above 30 MeV ($\text{pC}/\mu\text{m}$)	8.1	7.8
From Overdense Plasma (%)	100	70
From Underdense Plasma (%)	0	30
Estimated Total Charge above 30 MeV (pC)	101	83

Both cavities present a clean spectrum with a well defined peak in energy: 67 MeV with a FWHM spread of 6.2 MeV in the first cavity, and 37 MeV with a FWHM spread of 9.6 MeV in the second one. Nonetheless, the beam quality decreases in successive wakefield cavities, consistent with the expected degradation of the wakefield structure. Here, the beam quality is analyzed in terms of its FWHM energy spread, transverse size in the y direction, divergence (angle with respect to the x direction) and normalized rms (root mean square) emittance

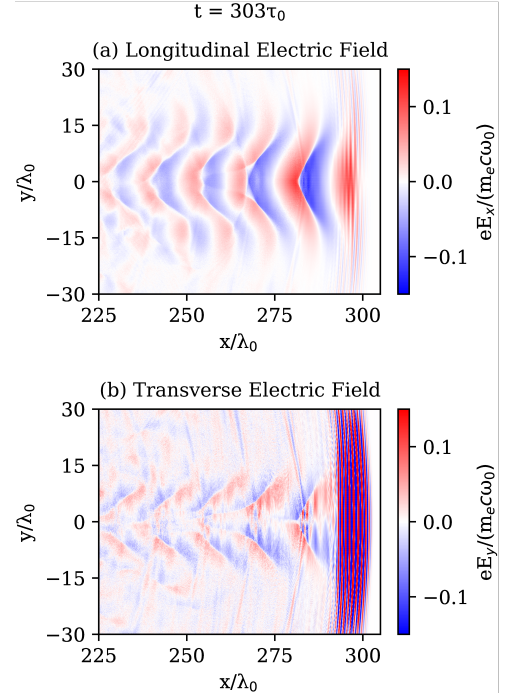


FIG. 4. Electric field in the (a) longitudinal x -direction and in the (b) transverse y -direction at $t = 303\tau_0$.

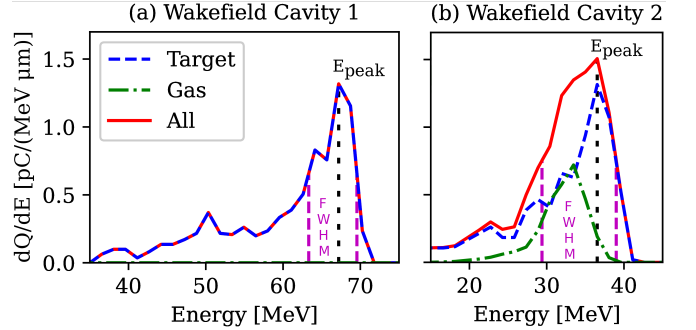


FIG. 5. Electron energy spectra in the (a) first and (b) second wakefield cavities at $t = 303\tau_0$. The dashed blue curve represents electrons from the overdense plasma (target), while the dash-dotted green curve shows electrons from the underdense plasma (gas). The solid red curve indicates the total electron population (all). The vertical dotted black line marks the peak energy, and the vertical dashed violet lines indicate the FWHM energy range.

given by

$$\text{emittance}_{\text{norm}} = \sqrt{\sigma^2(y)\sigma^2(p_y) - \langle y p_y \rangle^2} \quad (1)$$

where $\sigma^2(y)$, $\sigma^2(p_y)$ are the variances of y and p_y , and $\langle y p_y \rangle$ is the expected value of $y p_y$.

In the first cavity, the bunch reaches its highest peak energy (67 MeV) with a minimal relative spread (9.3%), forming a compact and spatially homogeneous beam (see Table I). All accelerated electrons originate from the overdense target. It yields lower FWHM

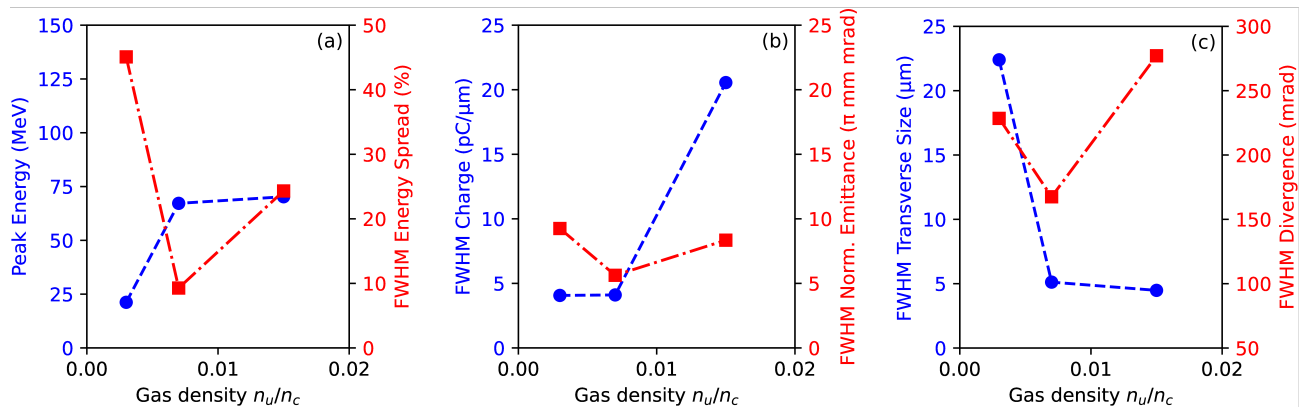


FIG. 6. Parametric study as a function of the normalized underdense plasma density n_u/n_c for electrons accelerated in the first wakefield cavity: (a) bunch peak energy (blue circles) and FWHM energy spread (red squares), (b) FWHM beam charge (blue circles) and FWHM normalized emittance (red squares), and (c) FWHM transverse size (blue circles) and FWHM divergence (red squares). The fixed parameters are $d = 0$, $L_H = 12\lambda_0 = 9.6 \mu\text{m}$ and $h = 10\lambda_0 = 8 \mu\text{m}$. The laser pulse has propagated a distance of $\sim 24\lambda_u$ in the underdense plasma region, which corresponds to a propagation time of $t = 457\tau_0$ for $n_u/n_c = 0.003$, $t = 303\tau_0$ for $n_u/n_c = 0.007$, and $t = 214\tau_0$ for $n_u/n_c = 0.015$.

divergence (168 mrad) and FWHM transverse size ($5.1 \mu\text{m}$), and a moderate FWHM normalized emittance (5.6π mm mrad). In the second cavity, the wake potential weakens: the peak energy is smaller (37 MeV) and the relative energy spectrum is broader, with a FWHM energy spread of 26%. The lower peak energy and the larger FWHM divergence (253 mrad) and FWHM transverse size ($7.7 \mu\text{m}$) reflect the partial wake degradation in the second cavity, but the bunch remains homogeneous and the normalized emittance is smaller (4.0π mm mrad).

We calculate the charge in the wakefield cavities in two ways: either by considering all the charge having an energy greater than 30 MeV (which is more or less half of the peak energy in the first cavity) as in Ref. [33], or by integrating the charge over the FWHM energy range shown in Fig. 5. The FWHM charge accounts for the spectrum useful for applications, such as medical, requiring low energy dispersion of the beam. While the charge above a certain energy level, 30 MeV for example, is important for applications requiring higher amounts of charge irrespective of the beam energy dispersion.

The total charge in 3D is next evaluated for both cases considering that electrons from the overdense plasma are emitted from a cylindrical aperture of radius $r = h/2$, which is also a conservative estimate for the minimum value of the wakefield cavities radius formed in the underdense plasma region. The cylindrical aperture emitting electrons from the overdense plasma has a circumference equal to $2\pi r$ in the yOz plane. While the underdense wakefield cavity has a transverse section of area πr^2 in the yOz plane. Thus, the charge in 3D is estimated by multiplying i) the 2D charge (integrated from the simulations in the xOy plane) originating from the overdense plasma by πr and ii) the 2D charge coming from the underdense plasma by $\pi r/2$. It is important to note that the 3D charge estimation considers a semi-circumference

and semi-circle area because the charge in 2D obtained from the simulations takes into account the overdense plasma aperture diameter h , as well as the underdense plasma wakefield cavity diameter in the y direction.

The charge values are reported in Table I. The first wakefield cavity accelerates a charge of $4.1 \text{ pC}/\mu\text{m}$ in the FWHM energy range, and $8.1 \text{ pC}/\mu\text{m}$ with energies above 30 MeV. The FWHM charge accelerated in the second cavity is higher since now the electrons come from both the overdense ($\sim 67\%$) and the underdense ($\sim 33\%$) plasma: $7.7 \text{ pC}/\mu\text{m}$. On the other hand, the charge with energies above 30 MeV is lower ($7.8 \text{ pC}/\mu\text{m}$) in the second cavity since the peak and maximum energies are also lower due to the partial wake degradation in this cavity.

IV. PARAMETRIC STUDY OF THE LASER-PLASMA INTERACTION

A parametric study was subsequently conducted to evaluate the impact of key parameters on the properties of the accelerated electron beams: the underdense plasma density n_u , the gap distance d between the overdense and underdense plasma, the overdense plasma length L_H , and the overdense plasma aperture diameter h . Figures 6-9 summarize the results for electrons accelerated in the first wakefield cavity (C1) after the laser pulse propagates a distance of $\sim 24\lambda_0/\sqrt{n_u/n_c}$ in the underdense plasma region, which corresponds to $t = 303\tau_0$ for the particular case $n_u = 0.007n_c$ and $L_H = 12\lambda_0$, with $\omega_u = \sqrt{n_u}e^2/\varepsilon_0 m_e$ the underdense plasma frequency and $\lambda_u = 2\pi c/\omega_u = \lambda_0\omega_0/\omega_u = \lambda_0/\sqrt{n_u/n_c}$ the underdense plasma wavelength. The high computational cost makes it prohibitive to carry out simulations for all the parameters until the electron beam reaches its maximum energy. However, it is important to note that the propagation

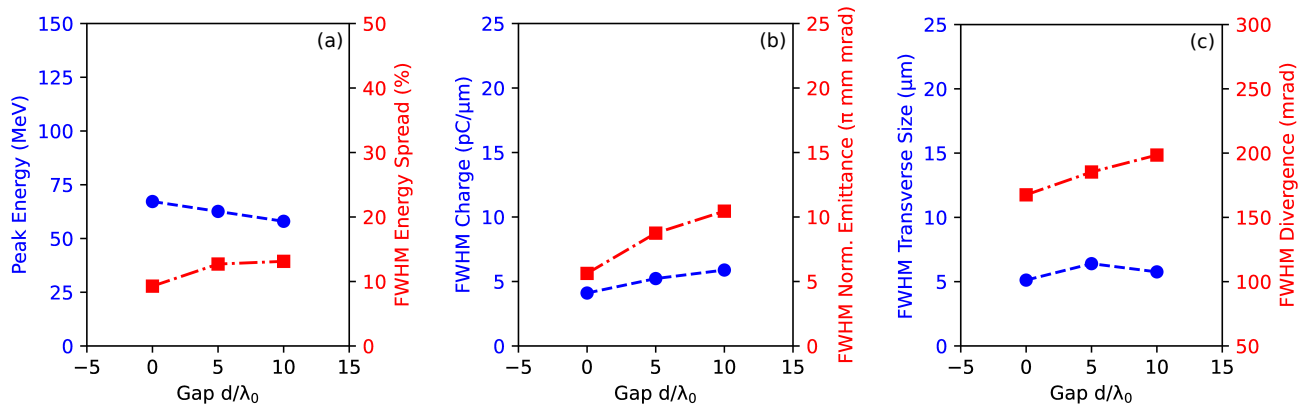


FIG. 7. Parametric study as a function of the normalized gap distance d/λ_0 between the overdense and underdense plasma for electrons accelerated in the first wakefield cavity: (a) bunch peak energy (blue circles) and FWHM energy spread (red squares), (b) FWHM beam charge (blue circles) and FWHM normalized emittance (red squares), and (c) FWHM transverse size (blue circles) and FWHM divergence (red squares). The fixed parameters are $n_u = 0.007n_c \simeq 1.2 \times 10^{19} \text{ cm}^{-3}$, $L_H = 12\lambda_0 = 9.6 \mu\text{m}$ and $h = 10\lambda_0 = 8 \mu\text{m}$. The laser pulse has propagated a distance of $\sim 24\lambda_u$ in the underdense plasma region, which corresponds to a total propagation time of $t = 303\tau_0$ for $d = 0$, $t = 308\tau_0$ for $d = 5\lambda_0$, and $t = 313\tau_0$ for $d = 10\lambda_0$.

distance considered ($\sim 24\lambda_0/\sqrt{n_u/n_c}$ in the underdense plasma) is long enough for the acceleration trends to be well established. This was verified in the case of some simulations running for longer times, as discussed in Section V. Thus, the tendencies in beam energy, charge and quality analyzed in this section continue to be observed up to the maximum energy that can be achieved by the electron beam.

The underdense plasma density n_u defines the underdense plasma wavelength $\lambda_u \propto n_u^{-1/2}$ and consequently determines the electron bunch capture location within the wakefield structure and energy transfer efficiency. The impact of varying n_u , while keeping the other parameters of the simulation unchanged, on the acceleration is presented in Fig. 6. Note here that fixing the laser propagation distance in the underdense plasma at $\sim 24\lambda_u$ and varying n_u causes the propagation time to vary as well: $t = 457\tau_0$ for $n_u/n_c = 0.003$, $t = 303\tau_0$ for $n_u/n_c = 0.007$, and $t = 214\tau_0$ for $n_u/n_c = 0.015$. From the scaling law in Ref. [41], the maximum energy gain scales as $(2/3)(n_c/n_u)a_0$, indicating that lower plasma densities allow for higher final energies. However, for the proposed injection mechanism, the peak energy increases from 21 MeV for $n_u/n_c = 0.003$ to 67 MeV for $n_u/n_c = 0.007$ and to 70 MeV for $n_u/n_c = 0.015$. The FWHM charge also increases with n_u , reaching 20.6 pC/μm for $n_u/n_c = 0.015$. In terms of beam quality, simulations show an optimal density at $n_u/n_c = 0.007$, where the beam achieves low values of FWHM energy spread (9%), emittance (5.6 π mm mrad), size (5.1 μm) and divergence (168 mrad). This is in accordance with the approximate optimal conditions for the bubble regime estimated in Ref. [41], which require a laser waist $W' \simeq (\sqrt{a_0}/\pi)\lambda_u \approx 8.5\lambda_0$ and a laser pulse duration τ' respecting $c\tau' \lesssim \lambda_u/2 \approx 6\lambda_0$. At lower and higher densities, the wakefield cavities do not form properly for effective

acceleration. At $n_u = 0.003n_c$, despite the theoretical energy advantage, the wakefield structure becomes insufficient for effective electron capture, such that the beam presents a low quality with a FWHM energy spread of 45%, size of 22.4 μm and divergence of 228 mrad. At $n_u = 0.015n_c$, the shorter plasma wavelength reduces the acceleration cavity size and worsens the beam quality, which presents a FWHM energy spread of 24% and divergence of 277 mrad. Thus $n_u/n_c = 0.007$ seems to be the better compromise for electron beam optimization and will be retained in the following.

Varying the gap d between the overdense and underdense plasma enables control over the relative position where target electrons are injected into the wakefield. This modifies the intensity of both longitudinal and transverse electric fields experienced by the injected electrons, directly affecting beam properties as shown in Fig. 7. Here once again the laser propagation distance in the underdense plasma is fixed at $\sim 24\lambda_u$. But this time, the total propagation time varies due to the different values of the gap distance d : $t = 303\tau_0$ for $d = 0$, $t = 308\tau_0$ for $d = 5\lambda_0$, and $t = 313\tau_0$ for $d = 10\lambda_0$. Increasing d from 0 to $10\lambda_0$ leads to a decrease in beam peak energy of approximately 14%, from 67 MeV to 58 MeV, and an increase in charge of 43%, from 4.1 pC/μm to 5.9 pC/μm, when considering the charge integrated over the FWHM energy range. Simultaneously, all the parameters related to the beam quality worsen. The FWHM energy spread increases from 9% to 13%, the FWHM normalized emittance doubles from 5.6 π mm mrad to 10.4 π mm mrad, the FWHM transverse beam size increases from 5.1 μm to 5.8 μm (with a maximum of 6.4 μm for $d = 5\lambda_0$), and the FWHM beam divergence increases 18%, from 168 mrad to 198 mrad. These results indicate that a smaller gap distance d favors higher beam energy and better beam quality (i.e., lower FWHM energy spread, emittance, beam size and divergence), while a larger d

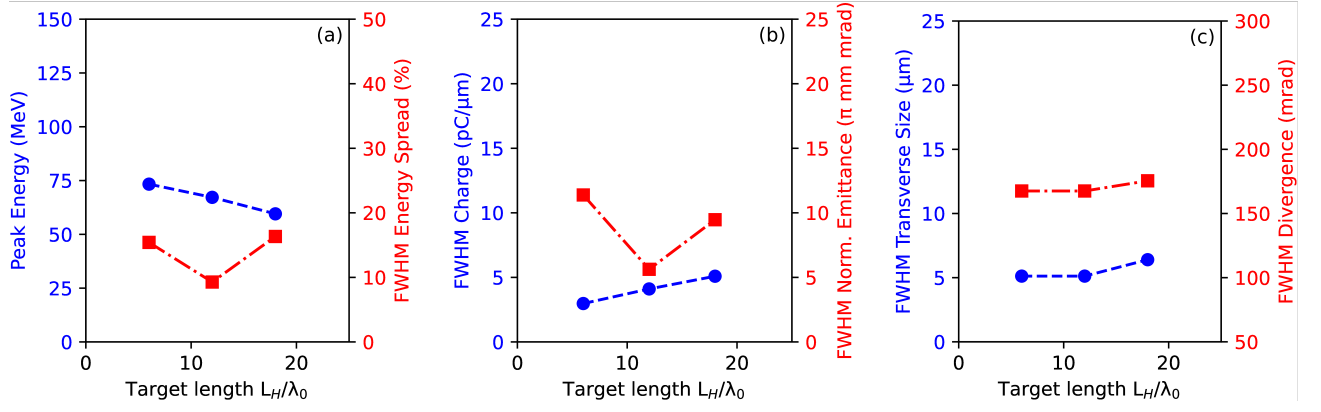


FIG. 8. Parametric study as a function of the normalized overdense plasma length L_H/λ_0 for electrons accelerated in the first wakefield cavity: (a) bunch peak energy (blue circles) and FWHM energy spread (red squares), (b) FWHM beam charge (blue circles) and FWHM normalized emittance (red squares), and (c) FWHM transverse size (blue circles) and FWHM divergence (red squares). The fixed parameters are $n_u = 0.007n_c \simeq 1.2 \times 10^{19} \text{ cm}^{-3}$, $d = 0$ and $h = 10\lambda_0 = 8 \mu\text{m}$. The laser pulse has propagated a distance of $\sim 24\lambda_u$ in the underdense plasma region, which corresponds to a total propagation time of $t = 298\tau_0$ for $L_H = 6\lambda_0$, $t = 303\tau_0$ for $L_H = 12\lambda_0$, and $t = 310\tau_0$ for $L_H = 18\lambda_0$.

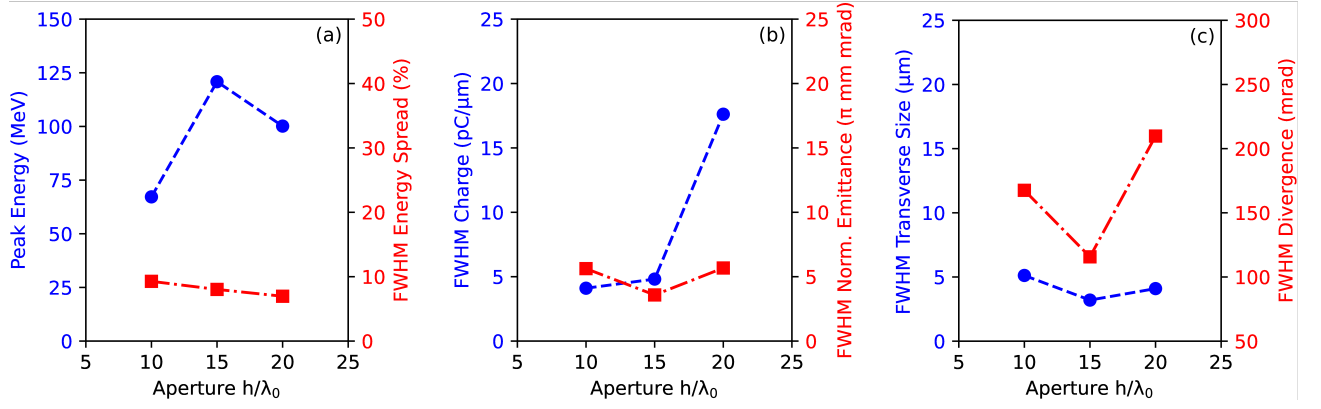


FIG. 9. Parametric study as a function of the normalized overdense plasma aperture diameter h/λ_0 for electrons accelerated in the first wakefield cavity: (a) bunch peak energy (blue circles) and FWHM energy spread (red squares), (b) FWHM beam charge (blue circles) and FWHM normalized emittance (red squares), and (c) FWHM transverse size (blue circles) and FWHM divergence (red squares). The fixed parameters are $n_u = 0.007n_c \simeq 1.2 \times 10^{19} \text{ cm}^{-3}$, $d = 0$ and $L_H = 12\lambda_0 = 9.6 \mu\text{m}$. The laser pulse has propagated a distance of $\sim 24\lambda_u$ in the underdense plasma region, which corresponds to a total propagation time of $t = 303\tau_0$ for all values of h .

enhances the beam charge at the expense of energy and beam quality.

Considering the overdense plasma alone, the energy gain of electrons extracted by the diffracted laser fields scales with $\sqrt{L_H}$, as discussed in Ref. [33]. This difference in energy modifies the electron injection position into the wakefield and the amount of charge that can be effectively captured and accelerated. The impact of varying L_H on the acceleration is presented in Fig. 8. Increasing L_H from $6\lambda_0$ to $18\lambda_0$ results in a 19% reduction in beam peak energy, from 73 MeV to 60 MeV, and a 71% increase in the FWHM charge, from 3.0 pC/ μm to 5.1 pC/ μm . It is important to notice that the initial energy of electrons extracted from the overdense plasma (which scales with $\sqrt{L_H}$ [33]) does not directly correlate with the final beam energy, as the injection position

within the wakefield plays a more important role. On the other hand, charge extraction increases at larger L_H values, which partially explains the reduction in final energy. The FWHM energy spread is ~ 15 -16% for $L_H = 6\lambda_0$ and $L_H = 18\lambda_0$, but reaches a minimum of 9% for $L_H = 12\lambda_0$. Similarly, the FWHM normalized emittance is about 9-11 π mm mrad for the lower and higher values of L_H , but it is minimized to 5.6 π mm mrad at $L_H = 12\lambda_0$. Both FWHM beam transverse size and FWHM divergence do not vary between $L_H = 6\lambda_0$ and $L_H = 12\lambda_0$, but increase for $L_H = 18\lambda_0$, passing from 5.1 μm to 6.4 μm , and from 168 mrad to 175 mrad respectively. *These results suggest that an optimal target length exists around $L_H = 12\lambda_0$, where a balance between beam energy, charge, size and divergence is achieved, along with improved energy spread and emittance.*

TABLE II. Beam parameters in the first wakefield cavity at maximum energy.

Parameter	$h = 10\lambda_0$	$h = 15\lambda_0$	$h = 20\lambda_0$	
			P1	P2
Time to reach Maximum Energy (τ_0)	893	973	686	
Maximum Energy (MeV)	180	278	224	
Peak Energy (MeV)	168	247	150	92
FWHM Energy Spread (MeV)	8.8	10.9	9.5	14.1
FWHM Energy Spread (%)	5.2	4.4	6.3	15.3
FWHM Divergence (mrad)	87	93	216	368
FWHM Transverse Size in y direction (μm)	4.6	3.6	4.1	7.2
FWHM Normalized Emittance (π mm mrad)	7.4	5.3	9.9	8.4
Integrated FWHM Charge ($\text{pC}/\mu\text{m}$)	4.3	5.9	16.6	24.2
From Overdense Plasma (%)	100	93	88	6
From Underdense Plasma (%)	0	7	12	94
Estimated Total FWHM Charge (pC)	54	107	393	322
Integrated Charge above 50 MeV ($\text{pC}/\mu\text{m}$)	8.0	19.9	105.6	
From Overdense Plasma (%)	100	76	34	
From Underdense Plasma (%)	0	24	66	
Estimated Total Charge above 50 MeV (pC)	101	329	1782	
Integrated Charge above 100 MeV ($\text{pC}/\mu\text{m}$)	8.0	19.9	62.7	
From Overdense Plasma (%)	100	76	55	
From Underdense Plasma (%)	0	24	45	
Estimated Total Charge above 100 MeV (pC)	101	329	1224	

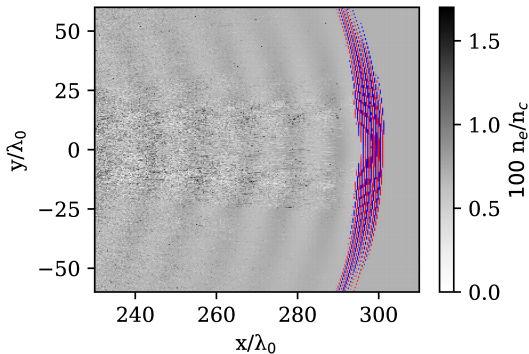


FIG. 10. Laser-plasma interaction showing the electron density (grayscale) and laser pulse (red/blue) in x - y space at $t = 303\tau_0$ for $h = 5\lambda_0$, $n_u = 0.007n_c \simeq 1.2 \times 10^{19} \text{ cm}^{-3}$, $d = 0$ and $L_H = 12\lambda_0 = 9.6 \mu\text{m}$.

The effect of the overdense plasma target aperture diameter h was also investigated and is presented in Fig. 9. For h smaller than $6\lambda_0$, a significant portion of the laser with beam waist $W = 9\lambda_0$ is blocked by the overdense plasma. The strong diffraction of the laser beam at the exit of the aperture prevents wakefield formation in the underdense plasma, as shown in Fig. 10 for $h = 5\lambda_0$, resulting in negligible electron acceleration. Conversely, when h greatly exceeds the laser waist W , insufficient electrons are extracted from the overdense plasma edges for effective injection, as was observed for $h = 30\lambda_0$. For moderate values of h , the aperture radius artificially imposes a waist on the laser pulse, changing the conditions for wakefield formation, particularly in the bubble

regime. It allows a balance between effective electron extraction from the overdense plasma and suitable wakefield formation for reasonable energy gain, beam charge and quality. Figure 9 shows that a maximum peak energy of 121 MeV is achieved for $h = 15\lambda_0 \sim 1.7W$, whereas the charge greatly increases for $h = 20\lambda_0 \sim 2.2W$, reaching $17.6 \text{ pC}/\mu\text{m}$ in the FWHM energy range. The FWHM energy spread decreases with h , from 9% for $h = 10\lambda_0$ to 7% for $h = 20\lambda_0$. The other quality parameters present a minimum at $h = 15\lambda_0$, where the FWHM beam emittance is 3.6π mm mrad, the FWHM size is $3.2 \mu\text{m}$ and the FWHM divergence is 116 mrad. *These results show that by varying the overdense plasma aperture diameter h it is possible to obtain the highest values of peak energy and FWHM charge while keeping a reasonable beam quality.*

V. OPTIMIZED LASER-PLASMA ELECTRON ACCELERATION

This section considers the parameters for which the electron beam presents a higher quality (*i.e.*, $n_u = 0.007n_c \simeq 1.2 \times 10^{19} \text{ cm}^{-3}$, $d = 0$ and $L_H = 12\lambda_0 = 9.6 \mu\text{m}$). As shown in Section IV, the overdense plasma aperture diameter h exerts the greatest influence on the maximum peak energy and maximum charge that can be achieved by the electron beam, and the trends observed in beam energy, charge and quality persist for longer time scales. For this reason, the role of parameter h in the acceleration process is further investigated in this section at the moment the beam achieves the highest peak energy.

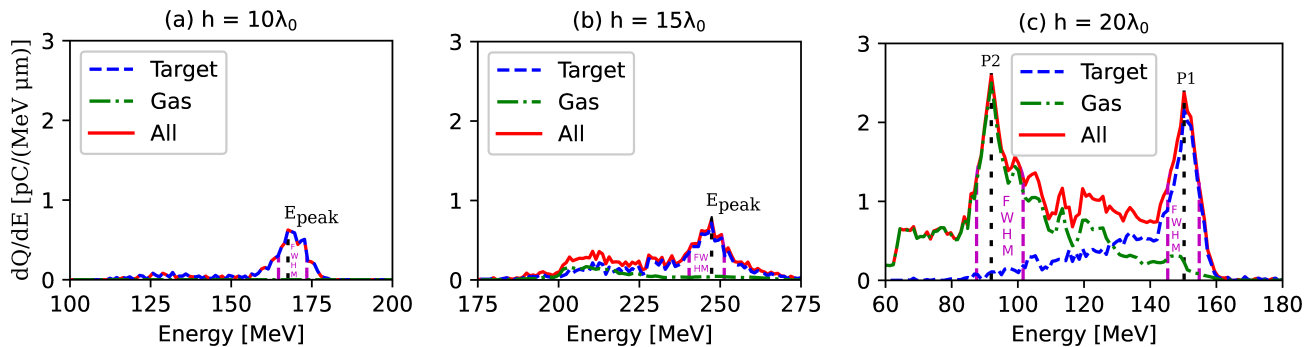


FIG. 11. Electron energy spectra in the first wakefield cavity at maximum peak energy for (a) $h = 10\lambda_0$, $t = 893\tau_0$, (b) $h = 15\lambda_0$, $t = 973\tau_0$, and (c) $h = 20\lambda_0$, $t = 686\tau_0$. The dashed blue curve represents electrons from the overdense plasma (target), while the dash-dotted green curve shows electrons from the underdense plasma (gas). The solid red curve indicates the total electron population (all). The vertical dotted black line marks the peak energy, and the vertical dashed violet lines indicate the FWHM energy range.

Table II summarizes the results, while Fig. 11 displays the respective energy spectra.

For $h = 10\lambda_0 = 8 \mu\text{m}$, the first wakefield cavity only captures electrons coming from the overdense plasma. At $t = 893\tau_0$, the electron beam reaches its maximum peak energy and its quality is significantly improved. Compared to earlier instants of time, as in Table I, the beam achieves notably higher maximum (180 MeV) and peak energies (168 MeV) and narrower relative FWHM energy spread (5.2%). Improved beam collimation is observed, indicated by a reduced FWHM divergence (87 mrad) and compact FWHM transverse profile (4.6 μm). These enhancements occur without compromising the beam charge (4.3 pC/ μm) integrated over the FWHM energy range, thereby improving the overall beam quality. Considering all the electrons accelerated to energies above 100 MeV, the charge is almost doubled, reaching 8.0 pC/ μm .

The beam maximum and peak energies greatly increase for $h = 15\lambda_0 = 12 \mu\text{m}$ and $t = 973\tau_0$, reaching 278 MeV and 247 MeV respectively. The amount of charge accelerated above 100 MeV is considerably higher (19.9 pC/ μm) since electrons coming from both the overdense ($\sim 76\%$) and underdense ($\sim 24\%$) plasma are now accelerated. Considering the FWHM charge, the great majority of electrons come from the overdense plasma ($\sim 93\%$) and only $\sim 7\%$ from the underdense plasma, totaling 5.9 pC/ μm . Despite the higher FWHM charge, the beam quality is enhanced, as can be seen by the lower relative FWHM energy spread (4.4%), FWHM transverse size (3.6 μm) and FWHM emittance (5.3 π mm mrad).

The electron beam reaches its maximum peak energy faster, at $t = 686\tau_0$, for $h = 20\lambda_0 = 16 \mu\text{m}$. The first cavity also accelerates electrons from the overdense and the underdense plasma. However, it presents two peaks (labeled P1 and P2 in Table II and Fig. 11(c)) in its energy spectrum. The peak energy P1 of 150 MeV is lower in this case when compared to smaller values of h . Even though the FWHM transverse size (4.1 μm) is comparable, the general beam quality is worse, presenting 6.3%

of relative FWHM energy spread, 216 mrad of FWHM divergence and 9.9 π mm mrad of FWHM normalized emittance. This deterioration in beam quality is due to the much higher FWHM charge accelerated in this peak: 16.6 pC/ μm , corresponding to an estimated 393 pC of FWHM charge in 3D.

While in the first peak (P1) $\sim 88\%$ of the accelerated electrons come from the overdense plasma, in the second energy peak (P2) only $\sim 6\%$ of the FWHM charge originates from the overdense plasma. Most of the charge ($\sim 94\%$) in the second peak comes from the underdense plasma, and it contains a comparable FWHM charge than P1: 24.2 pC/ μm , which corresponds to 322 pC in 3D. On the other hand, the peak energy and beam quality are reduced. The second peak P2 presents a peak energy of 92 MeV, with 15.3% of FWHM energy spread, 368 mrad of FWHM divergence and 7.2 μm of FWHM size.

Considering both energy peaks P1 and P2, the total charge accelerated to energies above 50 MeV and 100 MeV increases considerably, reaching 105.6 pC/ μm and 62.7 pC/ μm respectively, with an estimated 1782 pC and 1224 pC in 3D. These values are much higher than the ones for $h = 10\lambda_0$ and $h = 15\lambda_0$: 8.0 pC/ μm (101 pC in 3D) and 19.9 pC/ μm (329 pC in 3D) respectively.

The results in this section indicate that the proposed injection and acceleration scheme is effective at producing high-charge energetic electron beams over sub-millimeter distances. Furthermore, the overdense plasma aperture diameter h can be used as a control parameter to tune the beam properties, delivering higher energies around $h = 15\lambda_0$ and higher amounts of charge around $h = 20\lambda_0$.

VI. CONCLUSIONS

Different mechanisms exist for electron acceleration in plasmas. In the case of overdense plasmas, $\sim\text{nC}$ of charge can be achieved with a few MeV, but the beam presents a poor quality. Underdense plasmas, on the other hand, are

capable of accelerating electrons up to the GeV level with high quality, but the charge is low (a few pC). This paper presents an alternative electron acceleration scheme combining diffracted wave excitation from laser-overdense plasma interaction with wakefield generation in an underdense plasma. From 2D3V particle-in-cell simulations carried out with the SMILEI code, it was demonstrated that electrons extracted from the overdense plasma can be effectively injected into the underdense wakefield and accelerated to high energies, forming electron bunches with peak energies of $\sim 150 - 250$ MeV, estimated FWHM charge of $\sim 50 - 400$ pC, and $\sim 100 - 1800$ pC of charge with energies above 50 MeV.

Through a parametric study, the impact of key parameters on beam properties including peak energy, FWHM energy spread, charge, emittance, transverse size and divergence was analyzed. It was shown that the underdense plasma density plays an essential role in controlling the beam quality. A small gap distance between the overdense and underdense plasma produces beams with higher quality and higher energy, whereas increasing the gap distance increases the beam charge but reduces its energy and quality. Intermediate values of overdense plasma length allow for a better balance between beam energy, charge and quality.

The most important parameter analyzed for the proposed scheme is the overdense plasma aperture diameter h . For $h = 10\lambda_0$, only electrons coming from the overdense plasma are accelerated in the first wakefield cavity, reaching, at laser intensity $I_0\lambda_0^2 \simeq 3.4 \times 10^{19} \text{ W}\mu\text{m}^2/\text{cm}^2$, 168 MeV of peak energy with an estimated charge of 54 pC in the FWHM energy range and 101 pC with energies above 100 MeV. For higher values of h , electrons form both the overdense and the underdense plasma are accelerated in the first wakefield cavity. An aperture diameter of $h = 15\lambda_0$ produces the most energetic electron beams, with 247 MeV at peak, 107 pC of FWHM charge and 329 pC above 100 MeV. Increasing h to $20\lambda_0$ allows the acceleration of higher amounts of charge, reaching up to 1224 pC for energies above 100 MeV, but pro-

duces an energy spectrum with two energy peaks: one at 150 MeV with 393 pC of FWHM charge, and another one at 92 MeV and 322 pC of FWHM charge.

Understanding and optimizing the overdense and underdense plasma parameters enables the generation of electron beams with improved quality while maintaining substantial charge and high energy, offering an alternative approach for advanced electron sources. From the results presented in this paper, it appears that the parameters to be optimized depend on the choice between obtaining maximum energy or maximum charge.

Further optimization of this acceleration scheme is still possible and is currently in progress. Exploring a wider parameter space could enable the production of beams with improved quality, higher energy and/or higher charge. In particular, adding a transverse profile in the underdense plasma density would enable the laser to propagate as in a waveguide, thus allowing the study of the proposed mechanism while avoiding laser diffraction and depletion. Three-dimensional simulations would yield more precise electron beam charge values but require prohibitive computational resources, due to the need for high spatial resolution and high number of macro-particles per cell for accurate results.

ACKNOWLEDGMENTS

This project has received funding from the European Union's Horizon 2020 research and innovation programme under the Marie Skłodowska-Curie grant agreement No 899987, and Plas@Par Grant No. ANR-11-IDEX-0004-02. This project was provided with computing HPC and storage resources by GENCI at TGCC thanks to the grant 2013/2015/2017-0507678 on the supercomputer Joliot Curie's SKL and ROME partitions. Simulations were performed with the open-source particle-in-cell (PIC) code SMILEI . The authors are grateful to the TIPS-LULI team for fruitful discussions and to the SMILEI dev-team for technical support.

-
- [1] T. Tajima and J. M. Dawson, *Phys. Rev. Lett.* **43**, 267 (1979).
 - [2] E. Esarey, C. B. Schroeder, and W. P. Leemans, *Rev. Mod. Phys.* **81**, 1229 (2009).
 - [3] C. McGuffey, A. G. R. Thomas, W. Schumaker, T. Matsuoka, V. Chvykov, F. J. Dollar, G. Kalintchenko, V. Yanovsky, A. Maksimchuk, K. Krushelnick, V. Y. Bychenkov, I. V. Glazyrin, and A. V. Karpeev, *Phys. Rev. Lett.* **104**, 025004 (2010).
 - [4] A. Pak, K. A. Marsh, S. F. Martins, W. Lu, W. B. Mori, and C. Joshi, *Phys. Rev. Lett.* **104**, 025003 (2010).
 - [5] M. Chen, E. Esarey, C. B. Schroeder, C. G. R. Geddes, and W. P. Leemans, *Phys. Plasmas* **19**, 033101 (2012).
 - [6] J. P. Couperus, R. Pausch, A. Köhler, O. Zarini, J. M. Krämer, M. Garten, A. Huebl, R. Gebhardt, U. Helbig, S. Bock, K. Zeil, A. Debus, M. Bussmann, U. Schramm, and A. Irman, *Nat. Commun.* **8**, 487 (2017).
 - [7] P. Lee, G. Maynard, T. Audet, B. Cros, R. Lehe, and J.-L. Vay, *Physical Review Accelerators and Beams* **21**, 052802 (2018).
 - [8] A. Gonsalves, K. Nakamura, J. Daniels, C. Benedetti, C. Pieronek, T. de Raadt, S. Steinke, J. Bin, S. Bulanov, J. van Tilborg, C. Geddes, C. Schroeder, C. Tóth, E. Esarey, K. Swanson, L. Fan-Chiang, G. Bagdasarov, N. Bobrova, V. Gasilov, G. Korn, P. Sasorov, and W. Leemans, *Phys. Rev. Lett.* **122**, 084801 (2019).
 - [9] M. Kirchen, S. Jalas, P. Messner, P. Winkler, T. Eichner, L. Hübner, T. Hülsenbusch, L. Jeppe, T. Parikh, M. Schnepf, and A. R. Maier, *Phys. Rev. Lett.* **126**, 174801 (2021).
 - [10] S. Jalas, M. Kirchen, C. Braun, T. Eichner, J. Gonzalez, L. Hübner, T. Hülsenbusch, P. Messner, G. Palmer,

- M. Schnepf, C. Werle, P. Winkler, W. Leemans, and A. Maier, *Physical Review Accelerators and Beams* **26**, 071302 (2023).
- [11] P. Winkler, M. Trunk, L. Hübner, A. Martinez de la Ossa, S. Jalas, M. Kirchen, I. Agapov, S. A. Antipov, R. Brinkmann, T. Eichner, A. Ferran Pousa, T. Hülsenbusch, G. Palmer, M. Schnepf, K. Schubert, M. Thévenet, P. A. Walker, C. Werle, W. P. Leemans, and A. R. Maier, *Nature* **640**, 907 (2025).
- [12] S. C. Wilks, W. L. Kruer, M. Tabak, and A. B. Langdon, *Physical Review Letters* **69**, 1383 (1992).
- [13] P. Mora, *Physical Review Letters* **90**, 185002 (2003).
- [14] N. Naumova, I. Sokolov, J. Nees, A. Maksimchuk, V. Yanovsky, and G. Mourou, *Phys. Rev. Lett.* **93**, 195003 (2004).
- [15] J. Kupersztynch, M. Raynaud, and C. Riconda, *Physics of Plasmas* **11**, 1669 (2004).
- [16] N. M. Naumova, J. A. Nees, and G. A. Mourou, *Physics of Plasmas* **12**, 056707 (2005).
- [17] M. Raynaud, J. Kupersztynch, C. Riconda, J. C. Adam, and A. Héron, *Physics of Plasmas* **14**, 092702 (2007).
- [18] A. V. Arefiev, A. P. L. Robinson, and V. N. Khudik, *Journal of Plasma Physics* **81**, 475810404 (2015).
- [19] C. Riconda, M. Raynaud, T. Vialis, and M. Grech, *Physics of Plasmas* **22**, 073103 (2015).
- [20] M. Thévenet, A. Leblanc, S. Kahaly, H. Vincenti, A. Vernier, F. Quéré, and J. Faure, *Nature Physics* **12**, 355 (2016).
- [21] L. Fedeli, A. Sgattoni, G. Cantono, D. Garzella, F. Réau, I. Prencipe, M. Passoni, M. Raynaud, M. Květoň, J. Proška, A. Macchi, and T. Ceccotti, *Phys. Rev. Lett.* **116**, 015001 (2016).
- [22] A. Macchi, *Physics of Plasmas* **25**, 031906 (2018).
- [23] G. Cantono, A. Sgattoni, L. Fedeli, A. Denoëud, L. Chopineau, F. Réau, T. Ceccotti, and A. Macchi, *Physical Review Letters* **120**, 264803 (2018).
- [24] Z. Gong, A. P. L. Robinson, X. Q. Yan, and A. V. Arefiev, *Plasma Physics and Controlled Fusion* **61**, 035012 (2019).
- [25] M. Wen, Y. I. Salamin, and C. H. Keitel, *Phys. Rev. Appl.* **13**, 034001 (2020).
- [26] M. Jirka, M. Vranic, T. Grismayer, and L. O. Silva, *New Journal of Physics* **22**, 083058 (2020).
- [27] M. Raynaud, A. Héron, and J.-C. Adam, *Scientific Reports* **10**, 13450 (2020).
- [28] S. Marini, P. S. Kleij, F. Pisani, F. Amiranoff, M. Grech, A. Macchi, M. Raynaud, and C. Riconda, *Phys. Rev. E* **103**, L021201 (2021).
- [29] S. Marini, P. S. Kleij, F. Amiranoff, M. Grech, C. Riconda, and M. Raynaud, *Physics of Plasmas* **28**, 073104 (2021).
- [30] X. Shen, A. Pukhov, S. Perevalov, and A. Soloviev, *Quantum Electronics* **51**, 833 (2021).
- [31] J. Sarma, A. McIlvenny, N. Das, M. Borghesi, and A. Macchi, *New Journal of Physics* **24**, 073023 (2022).
- [32] P. K. Singh, F.-Y. Li, C.-K. Huang, A. Moreau, R. Hollinger, A. Junghans, A. Favalli, C. Calvi, S. Wang, Y. Wang, H. Song, J. J. Rocca, R. E. Reinovsky, and S. Palaniyappan, *Nature Communications* **13**, 54 (2022).
- [33] S. Marini, M. Grech, P. S. Kleij, M. Raynaud, and C. Riconda, *Phys. Rev. Res.* **5**, 013115 (2023).
- [34] X. F. Shen, A. Pukhov, and B. Qiao, *Phys. Rev. X* **11**, 041002 (2021).
- [35] S. V. Bulanov, N. Naumova, F. Pegoraro, and J. Sakai, *Phys. Rev. E* **58**, R5257 (1998).
- [36] T. P. Rowlands-Rees, C. Kamperidis, S. Kneip, A. J. Gonsalves, S. P. D. Mangles, J. G. Gallacher, E. Brunetti, T. Ibbotson, C. D. Murphy, *et al.*, *Phys. Rev. Lett.* **100**, 105005 (2008).
- [37] G.-B. Zhang, Y.-Y. Ma, H. Xu, N. A. M. Hafz, X.-H. Yang, M. Chen, T.-P. Yu, D.-B. Zou, J.-X. Liu, J.-F. Yan, H.-B. Zhuo, L.-F. Gan, L.-C. Tian, F.-Q. Shao, Y. Yin, and S. Kawata, *Physics of Plasmas* **22**, 083110 (2015).
- [38] L. Fedeli, A. Huebl, F. Boillod-Cerneux, T. Clark, K. Gott, C. Hillairet, S. Jaure, A. Leblanc, R. Lehe, A. Myers, C. Piechurski, M. Sato, N. Zaïm, W. Zhang, J.-L. Vay, and H. Vincenti, *SC22: International Conference for High Performance Computing, Networking, Storage and Analysis*, 1 (2022).
- [39] J. Derouillat, A. Beck, F. Pérez, T. Vinci, M. Chieramello, A. Grassi, M. Flé, G. Bouchard, I. Plotnikov, N. Aunai, J. Dargent, C. Riconda, and M. Grech, *Comput. Phys. Commun.* **222**, 351 (2018).
- [40] R. Nuter, M. Grech, P. Gonzalez de Alaiza Martinez, *et al.*, *European Physical Journal D* **68**, 177 (2014), received 28 February 2014, Revised 14 April 2014, Published 27 June 2014.
- [41] W. Lu, M. Tzoufras, C. Joshi, F. S. Tsung, W. B. Mori, J. Vieira, R. A. Fonseca, and L. O. Silva, *Physical Review Special Topics - Accelerators and Beams* **10**, 061301 (2007).